A Peristaltic Soft, Wearable Robot for Compression Therapy and Massage

Mengjia Zhu [ID], Adrian Ferstera, Stejara Dinulescu, Nikolas Kastor [ID],
Max Linnander [ID], *Graduate Student Member, IEEE*, Elliot W. Hawkes, and Yon Visell [ID], *Member, IEEE*

Abstract—Soft robotics is attractive for wearable applications that require conformal interactions with the human body. Soft wearable robotic garments hold promise for supplying dynamic compression or massage therapies to improve lymphatic and blood circulation. In this letter, we present a wearable robot capable of supplying dynamic compression and massage therapy via peristaltic motion of finger-sized, soft, fluidic actuators. We show that this peristaltic wearable robot can supply dynamic compression pressures exceeding 22 kPa at frequencies of 14 Hz or more, meeting requirements for compression and massage therapy. A large variety of software-programmable compression wave patterns can be generated by varying frequency, amplitude, phase delay, and duration parameters. We finally demonstrate the utility of this peristaltic wearable robot for compression therapy, showing fluid transport in a laboratory model of the upper limb. We theoretically and empirically identify driving regimes that optimize fluid transport. These findings show the potential of such a wearable robot for the treatment of several health disorders associated with lymphatic and blood circulation, such as lymphedema and blood clots.

Index Terms—Soft robot applications, wearable robotics.

I. INTRODUCTION

EMERGING soft robotic technologies are becoming widely investigated for applications in health and medicine, as they are well-suited for delivering dynamic compression or massage therapy. Such therapies, when administered by a health professional, are effective in treating blood and lymphatic circulatory disorders, including chronic venous insufficiency (CVI), venous ulcers, lymphedema, and blood clots [1], [2], as well as for treating musculoskeletal injuries [3].

A. Design Considerations for Compression Therapy Devices

Compression therapy devices are expected to meet functional requirements arising from therapeutic standards that help ensure efficacy and safety or otherwise conform to norms of massage practice. Such guidelines are necessarily application-specific. Compression therapies requiring gross occlusion of venous blood flow in the lower limbs demand substantial compression pressures, amounting to 3.3 kPa, 8.0 kPa, or 9.3 kPa in the supine, sitting, or standing positions respectively [4]. In other applications, massage therapies are supplied for mild pain relief, easing of musculoskeletal tension, or touch-supplied (i.e., haptic) emotional comfort. Examples include sports, Swedish, kinesiology, or deep tissue massage. Such practices can involve the application of light to firm pressures, ranging from less than 12 kPa to 30 kPa or more [5].

Wearability introduces further requirements that arise from ergonomics and safety. To ensure comfort, compression garments should be soft, low-profile, and compliant. To avoid pain, injury, or lesions damaging soft tissues, static and dynamic forces should be distributed to avoid stress concentrations. For devices that emulate manual massage, it may be appropriate that compression is supplied via individually actuatable modules the size of a finger or hand.

B. Background and Motivation

The most established technologies meeting some of the needs mentioned are intermittent pneumatic compression devices (IPC) [6]. Studies have shown that such devices can reduce the incidence of venous thromboembolism (VTE) [7] and promote greater lymphatic flow than other modes of treatment [8].

A common feature of these devices is that they rely on pneumatic inflation of the bladders to exert compression pressure on the skin, making them bulky in size. The smallest width of the individual pneumatic bladder unit reported in the literature is 4.5 cm used for human limbs [12] (Table I). Comerota argued that using smaller-sized bladders in IPC devices may help with generating a transiently high venous velocity because it is easier to achieve rapid pressure rise [14]. Additional benefits of a low-profile device include enabling mobile use scenarios where the user could wear the device while walking and doing daily tasks.

Low-profile compression therapy devices also hold promise for pediatric applications, where about 5% of the population are
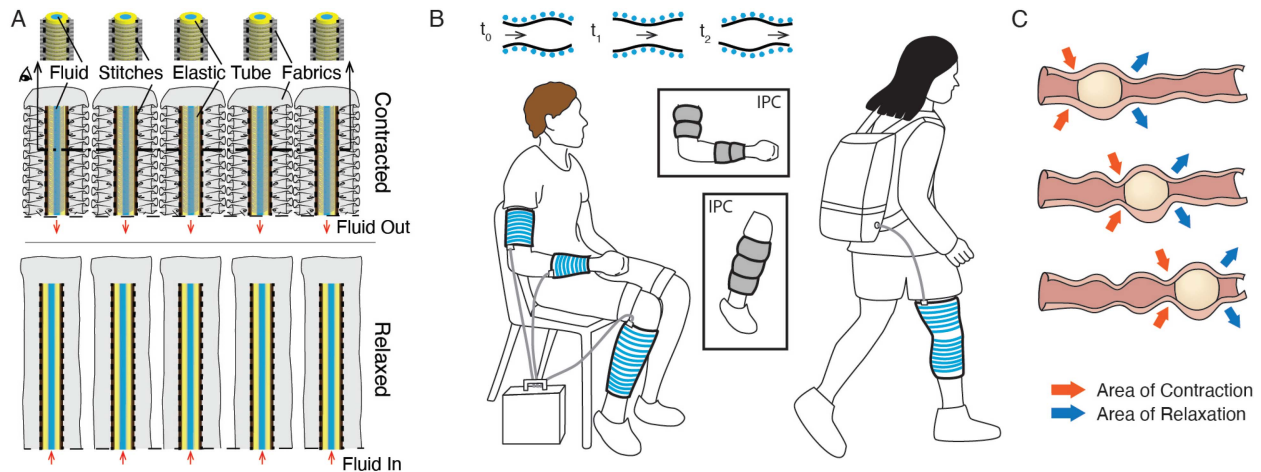
Fig. 1. (a) FFMS actuators are used for the peristaltic wearable robot design. These actuators are arranged in parallel to mimic peristalsis. (b) Our peristaltic wearable robot can be used in various body locations and mobile use cases. The top insert demonstrates the propagation of the peristaltic wave generated. Compared to conventional IPC devices (middle inserts), our peristaltic wearable robot is significantly more compact. (c) Peristaltic transport in biological organs such as the digestive tract involves sequential contraction and relaxation of muscles.

TABLE I
SELECTED METRICS OF COMPRESSION THERAPY DEVICES REPORTED IN THE LITERATURE

Reference	Unit width	Number of units	Actuation type
Zhu et al. (This work)	1 cm	8	Hydraulic
Zhao et al. [9]	6.5 cm	6	Pneumatic
Manfredini et al. [10]	13 cm	1	Pneumatic
John et al. [11]	9 cm	3	Pneumatic
Payne et al. [12]	4.5 cm	3	Pneumatic
Olszewski et al. [13]	9 cm	8	Pneumatic

affected by vascular anomalies [15]. A recent review of clinical experiences and treatments on venous thromboembolism in pediatric groups shows that the standard compression therapy treatment is passive compression garments [15]. IPC devices that are designed for adults are not readily adaptable to pediatric applications, as argued by authors of the only prior such study, which itself yielded inconclusive outcomes [16]. More compact compression IPC devices, like that reported here, could facilitate clinical studies of the efficacy of IPC therapies for pediatric patients.

Existing devices using pneumatic actuation are often energetically inefficient, due to thermodynamic losses arising from gas compression cycles [17]. Although hydraulic systems experience viscous losses, these losses may not be as large as the thermodynamic losses that occur in pneumatic systems. In our previous research, we compared the efficiencies of hydraulic and pneumatic actuator operations and found that hydraulic operation yielded higher efficiency (R = 0.46) compared to pneumatic operation (R = 0.25) [17]. Energy efficiency is very important for the design of portable and mobile devices, where the power source is provided by batteries. Pneumatic actuators also store substantial energy in gas compression, which can pose hazards upon soft material failure, due to rapid energy release. There is a need to investigate alternative actuation methods for portable and mobile applications.

Other researchers have studied the effect of IPC driving stimuli for venous and lymphatic flow [18], [19]. However, none of them justified the findings with theoretical predictions based on the peristaltic mechanism. The modeling of IPC devices has been focusing on the fluid-structure coupling model [20], with little information on wave characteristics which are crucial for the control optimization of these devices. Additionally, prior studies with IPC devices employed either low frequencies (0.5 Hz) or very low frequencies (≤ 0.2 Hz), likely due to design constraints [18], [21]. Thus, the effects of IPC using higher frequencies remains unknown. Although these low-frequency compression therapies are effective at promoting blood flow, the potential benefits of using higher frequencies for blood flow promotion have not been studied with IPC devices for humans.

C. Contributions

Here, we report a low-profile compression therapy device that has a unit width of 1 cm, enabling applications requiring compact size such as for pediatric uses. We incorporate energy efficiency considerations by using hydraulic operations that could support applications in mobile use cases (Fig. 1). We integrate design and modeling to study the effect of frequency, wavelength, and fluid viscosity by cross-validating theoretical models with experimental results. We present the design, fabrication, modeling, and evaluation of the peristaltic wearable robot and the associated control system. Characterization results show that the system we designed can supply compression pressures as large as 22 kPa with frequencies up to 14 Hz, meeting the requirements for compression and massage therapy, as determined in prior literature [4], [12], [18]. Our proof-of-concept demonstration for compression therapy shows that this peristaltic wearable robot is capable of driving venous flow in an artificial limb with the flow rate increasing linearly with peristaltic wavelength and frequency, consistent with our theoretical predictions based on wave mechanics.

This work provides a novel and compact method for supplying compression therapy that could treat venous and lymphatic inefficiencies. This work helps gain insights into the mechanism of IPC-like treatment and offers guidelines for optimal device design and operation.

II. DEVICE DESIGN AND OPERATING PRINCIPLE

We demonstrate a soft wearable robot that generates massage-like motions on the human limb through dynamic compression waves based on peristalsis for mobile applications (Fig. 1). Peristalsis is a biological transport mechanism produced via sequential contraction of muscles, as found in the esophagus [22], uterus [23], ureter [24], or blood vessels [25]. Media within a peristaltic channel is transported by radially symmetric wave motion of the channel walls (Fig. 1(c)).

A. Wearable Design and Fabrication

The peristaltic wearable robot creates dynamic compression force patterns on the wearer's limbs (Fig. 1(b)). It is fabricated with eight fluidic fabric muscle sheet (FFMS) actuators (Fig. 1(a)), described in our recent publications [17], [26], [27]. Due to their modularity in fabrication size and tube diameter, these actuators can be made as small as 1 cm in width, resembling the width of human fingers (Table I). Our low-profile wearable robot can make compression therapy accessible for pediatric users with smaller limbs. Several alternative actuators are available, including Inverse Pneumatic Artificial Muscles (IPAM) [28], soft hydraulic filament artificial muscles [29], and thin McKibben Muscles [30], [31]. Here, we elected to use FFMS actuators due to their easy fabrication process, hydraulic operation, and ability to generate a wide range of displacements and forces.

The operating principle of FFMS is elaborated in detail in our previous work [17]. When fluid pressure is high, the actuator extends to its longest state. When the fluid pressure decreases, the actuator contracts and exerts forces on the payload (Fig. 1(a)). When wrapped around a human limb circumferentially, each actuator is capable of supplying localized compressive pressure to the limb. This working principle is intrinsically different from the IPC devices, such that a compact-sized FFMS actuator may still supply large compression pressures. The parallel arrangement of multiple actuators makes it possible to provide spatial-temporal compression patterns, including wave-like patterns that produce peristalsis.

We fabricated the actuators using the methods described in Zhu et al. [17]. The geometry of the soft latex tubing used inside the fabric conduits affects the fluid pressure required to fully operate the actuator, as well as the maximum compression force generated [17]. The actuator length should be designed such that the actuator can wrap around the human limb and produce compression pressure of at least 9.3 kPa for compression therapy [4]. Based on these requirements and the analytical modeling in Zhu et al. [17], we specified the tubing to have an outer diameter of 4.8 mm, and an inner diameter of 3.2 mm. We selected the stitching length as 177 mm and the wrinkling ratio was 2.5. The fabricated actuators were then pre-pressurized and hand-sewn onto a stretchable sleeve for comfort using a zig-zag
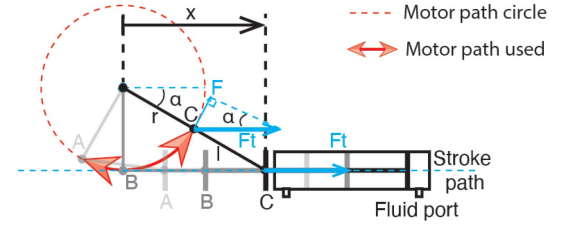

Fig. 2. Schematic design of the slider-crank driving mechanism.

pattern that preserves stretchability. The sleeve with all actuators weighs 0.05 kg.

B. Design and Modeling of the Fluid Driving System

We created a customized modular system to supply hydraulic pressure for FFMS actuators, as hydraulic actuation has been proven to have higher efficiency than pneumatic actuation methods [17]. The system uses compact, servo-driven, hydraulic cylinders (Bimba 013-D, with a bore diameter of 11 mm and a maximum stroke of 76 mm) to drive the fluid (water). We implemented systems based on either two or eight motorized cylinders, as described below. A slider-crank linkage is chosen over linear screws for higher actuation speed to convert the rotary motion to linear motion. The max, neutral, and minimum stroke positions are illustrated as A, B, and C in Fig. 2, with $l = r$ and $\alpha = 30°$. In a quasi-static condition, the input torque τ of the motor can be related to the output fluid pressure p by:

$$\tau = rF_t \sin \alpha = rpA_i \sin \alpha, \ 30° \leq \alpha \leq 120° \quad (1)$$

Here, F_t is the output force acting on the piston rod of the hydraulic cylinder and A_i is the inner cross-sectional area of the hydraulic cylinder. The relationship between the crank angle α and the piston location x is obtained from the kinematics of a fourbar offset slider-crank [32]:

$$x = r \cos \alpha + l \sqrt{1 - \left(\frac{r \cdot \sin \alpha - r}{l} \right)^2}, \ 30° \leq \alpha \leq 120° \quad (2)$$

We designed a two-motor system to produce peristaltic motions via quadrature driving of eight hydraulic channels using two motorized cylinders (Fig. 3(a) and (c)). When two sinusoidal signals with a phase delay of $\pi/2$ drive the two motors, a compression force pattern similar to a sinusoidal wave is spatially generated along the wearable robot (Fig. 3(a)). Different input signals result in distinct spatiotemporal compression force patterns (Fig. 3(b)).

The two-motor compact design uses a minimal number of motors at the cost of coupled compression forces. It measures 5 cm (width) x 30 cm (length) x 5 cm (height) and weighs 1.76 kg. The mass of this system is lighter than a half-gallon of water (1.9 kg). The entire driving system, including the fluid and electric sources, can be assembled in a compact package that is easy to carry or wear during daily activities. The two-motor system is preferred when a compact driving system is the highest priority. To accommodate use cases where each hydraulic channel needs to be controlled independently, we further designed an eight-motor driving system that can generate arbitrary compression force patterns (Fig. 3(d) and (e)). The
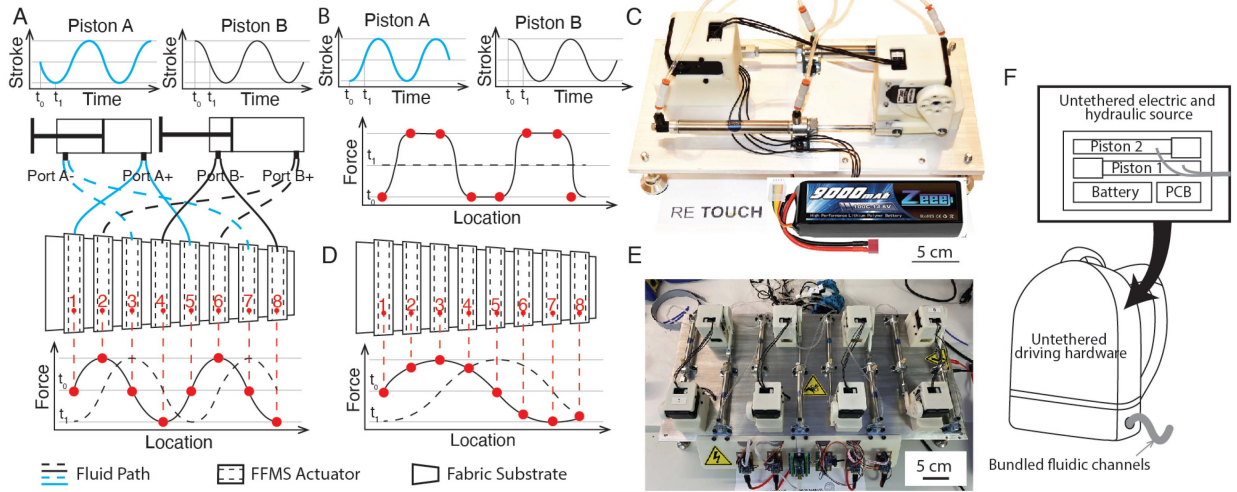
Fig. 3.   Various control input designs can be used to generate spatiotemporal compression wave patterns. (a) Two pistons can control eight actuators for maximum efficiency, with spatial compression forces coupled at locations routed to the same motor. The sinusoidal displacements with a phase delay of $\pi/2$ on the top denote an example of the input signal for both pistons. The plot on the bottom illustrates the resulting spatial profile of the compression force at times t_0 and t_1. (b) The two-piston driving system can also compose other spatial-temporal compression force patterns, with the top figures showing the piston input signals, and the bottom figure showing the composed spatiotemporal waves. (c) The prototype of the two-piston driving system with a battery shown in scale. (d) The driving system can be expanded to eight pistons to control each actuator independently. Arbitrary spatial compression force waves can be generated. (e) The prototype of the eight-piston driving system. (f) The driving system could be further reduced in size by using a compact design of hydraulic system, a compact battery, and custom printed circuit board (PCB) for control signals.

eight-motor system measures 30 cm (width) x 60.5 cm (length) x 8 cm (height) and weighs 6.92 kg. The driving system could be further reduced in size by using compact components and higher-density packing strategies (Fig. 3(f)).

With the eight-piston driving system, peristaltic compression patterns are generated when each cylinder was driven sinusoidally with an onset delay time of Δt between adjacent actuators:

$$\alpha = A \sin\left(2\pi f(t + (n-1)\Delta t) \right), \tag{3}$$

where α is the rotation degree for the motor, n indexes the actuator channel, t is the time variable, A and f are the amplitude and frequency of the sinusoidal wave respectively. The spatial wave generated by all the actuators is described as:

$$y(x,t) = A' \cos\left(\frac{2\pi}{\lambda}x - 2\pi f(t - \Delta t) \right), \tag{4}$$

where y and x are the vertical and horizontal position variables, A' is the amplitude of the spatial wave, and λ is its corresponding wavelength.

C. Control Software and Interface

Each piston is driven by a programmable high torque servo (HerklueX DRS 0602, DST Robot) that is controlled by computer via a synchronous serial communication. A software graphical user interface (GUI) enables the design of compression patterns via frequency, amplitude, duration, and phase parameters. The motors can be powered using a rechargeable Lipo battery (14.8 V, 9 A).

III. MECHANICAL CHARACTERIZATION OF THE DYNAMIC COMPRESSION SYSTEM

Various peristaltic, all-in-phase, and sequential spatiotemporal compression patterns can be delivered through time-varying signals for a single actuator, as well as multiple actuators at different locations. In this section, we evaluate the compression force generated by a single actuator, the dynamic frequency response of the system, and the large range of dynamic compression motion patterns that the peristaltic wearable robot is capable of generating.

A. Single Actuator Compression Force and Frequency Response Evaluation

We characterized the compression force of a single actuator by wrapping it around a cylindrical testing fixture with a force sensor (ATI Nano17; ATI Industrial Automation). The force sensor measures part of the compression force exerted on an arc segment with a central angle of 68.9 degrees. The diameter of the cylinder in the testing setup is 63.7 mm to mimic the size of a human limb. Different design parameters of the testing fixture, such as the cylinder radius, can affect the compression pressure measurement. The compression pressure can be linked to the hoop stress as follows:

$$P_c = \frac{t_{act}\sigma_{act}}{R} = \frac{F}{A_c}, \tag{5}$$

where P_c represents the compression pressure, t_{act} and σ_{act} are the thickness and the axial stress of the actuator, R is the radius of the cylinder wrapped by the actuator, F is the force measured from the ATI nano 17, A_c is the contact area between the actuator and the testing cylinder. A position encoder measured the instantaneous stroke of the hydraulic cylinder, and a pressure sensor was used to monitor hydraulic pressure. All
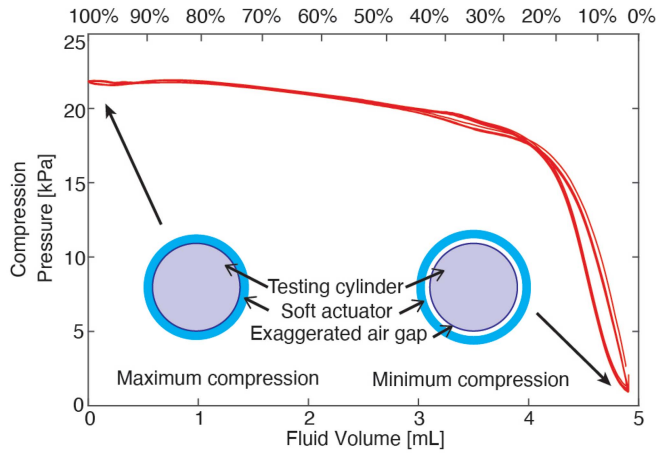
Fig. 4. Relationship between fluid volume and compression pressure follows a similar curve for different operation strokes ranging from 10% to 100%. Superposed compression volume curves for driving stroke amplitude from 10% to 100% (labeled on the top x axis) show that the curves nearly superpose with each other. Note that the minimum compression pressure occurs when the fluid volume is maximum. As the fluid is withdrawn from the actuator, the compression pressure increases. The inserted diagrams illustrate the extreme conditions for maximum and minimum compression pressure to occur.

sensing signals were recorded synchronously using a real-time computer-in-the-loop system with a sampling rate of 100 Hz (QPIDe; Quanser, Inc., with Simulink, The MathWorks, Inc.).

Results showed that compression pressure decreased with increasing fluid volume in the actuator, which is consistent with the model presented in Zhu et al. [17] (Fig. 4). The resting state of the actuator is when the fluid volume is maximum, leading to minimum compression pressure. When fluid volume is withdrawn from the actuator, the compression pressure increases. This relationship was approximately linear both before and after fluid volume of 4 mL, with a larger slope for fluid volume between 4 mL and 5 mL. The maximum compression pressure decreased with operation stroke range, as the margins illustrated in Fig. 4. This behavior is likely related to the elasticity of the tubing.

We evaluated the system's dynamic frequency response at frequencies ranging from 0.2 Hz to 50 Hz with stroke amplitudes from 10% to 100%. The stroke of the piston was measured, and the actual frequency (experimental frequency) was obtained using spectral analysis of the data. Fig. 5(a) shows the results for the stroke amplitude of 10% across frequencies ranging from 0.2 Hz to 50 Hz using the same testing setup shown in Fig. 4. Compression pressure decreased as frequency increased up to 17 Hz, above which the compression pressure and the fluid volume had similar ranges. We observed hysteresis losses, which we mainly attributed to hydrodynamic flow resistance, dry friction at the tube-fabric interface, and elastic hysteresis caused by internal material friction of the stretchable tubing [17]. Results also revealed that the system was capable of operating at frequencies up to 20 Hz (Fig. 5(b)). Motor power constrained the stroke amplitude in that the lower the maximum stroke used, the higher frequency achieved. The magnitude decrement was more prominent for larger maximum stroke (Fig. 5(c)), while little magnitude decrement was observed when operating with 10% stroke.

B. Dynamic Compression Motion Patterns

We characterized the dynamic spatial compression motion patterns by measuring shape deformation with an optical motion capture system (Flex 13; OptiTrack). Twenty-four reflective markers (5 mm diameter) were distributed on the surface of the wearable robot, with three on each actuator (Fig. 6(a)). The peristaltic wearable robot was wrapped around a soft foam cylinder with a diameter of 76.2 mm (McMaster-Carr). Compression patterns were generated and the dynamic positions of each marker are measured. Fig. 6(b)–(f) shows the average radius changes of the three markers on each actuator over time. We composed five peristaltic motion patterns by varying the wavelength, wave speed, and starting actuator. Two examples of these patterns are shown in Fig. 6(b) and (c). Additionally, we generated an all-in-phase synchronized compression pattern (Fig. 6(f)). We also evaluated two sequential compression patterns, with compression durations of 1 s and 2 s, respectively (Fig. 6(d) and (e)). In both cases, the onset delay time between actuators for sequential actuation was 1 s. The applied compression produced a radial compression around the soft foam cylinder. We observed modest variations in the magnitude of radial contraction, which could be attributable to variations in the mechanics of the soft foam cylinder, coupling of the actuated tube to the soft foam cylinder, or measurement artifacts. These results mechanically validated that the wearable robot was capable of generating different compression patterns on a soft body.

IV. APPLICATION FOR COMPRESSION THERAPY AND THERAPEUTIC MASSAGE

Such a peristaltic wearable robot holds promise for compression therapy to promote blood circulation and for therapeutic massage. Peristaltic action on a flexible tube can introduce fluid flow, and can thus be used to promote blood flow in the veins to treat various medical conditions [1], [2], [3]. To demonstrate the ability of the peristaltic compression robot to promote blood circulation, we designed and fabricated an upper arm model (Fig. 7(b)) that mimics the anatomy of the human upper arm (Fig. 7(a)) [33]. This design method is similar to an artificial lower limb model used for a fluid-structure coupling study [20]. The muscles (triceps, biceps, and brachialis muscles) and skin were realized and modeled using a soft silicone material (Ecoflex 00–30, shore hardness 00–30, Smooth-On, Inc., Macungie, PA). A rigid 3D-printed bone structure was fabricated in CPE (Ultimaker filament). A latex tube was placed adjacent to the bone, representing the brachial vein. A soft strip made of stiffer silicone with a shore hardness of 2 A (Dragon Skin FX-Pro, Smooth-On, Inc., Macungie, PA) was used to direct compression pressure to the vein.

The limb apparatus is shown in Fig. 7(c). Vegetable glycerin served as the fluid for transport in the artificial vein, as it can be mixed with water for different viscosity values [36].

The peristaltic compression robot was wrapped around the limb model, with a spacing of about 1.1 cm between adjacent actuators. During peristaltic actuation, a flow was induced, transporting fluid from the source through an elbow connector to the collection container (Fig. 7(c)). From the theory of peristaltic flow in tubes [34], when the pressure change over one wavelength is zero, $\Delta P_\lambda = 0$, such that the driving pressure is
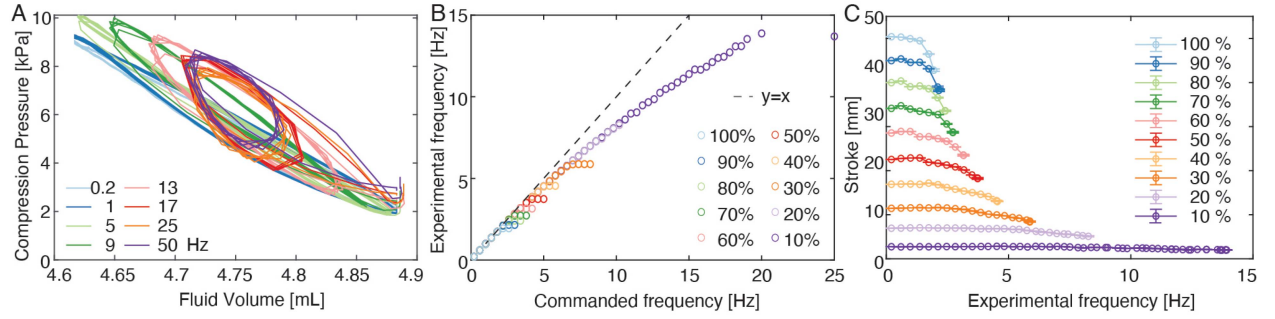
Fig. 5. Frequency response of the system. (a) The hysteresis loops presented in the relationship between fluid volume and compression pressure show energy loss during the actuation. The energy loss increases with increasing frequency. Legend: commanded frequency in Hz. (b) Legend: different operation stroke range in %. The experimental frequency reaches a plateau for all stroke ranges. The smaller the stroke range, the higher the experimental frequency achieved. Overall, the system is able to operate at frequencies up to about 20 Hz despite some discrepancies between commanded frequency and experimental frequency. (c) As the stroke magnitude gets higher, the drop-off in stroke occurs at lower frequencies. The magnitude remains almost flat across all frequencies for 10% operation stroke range.
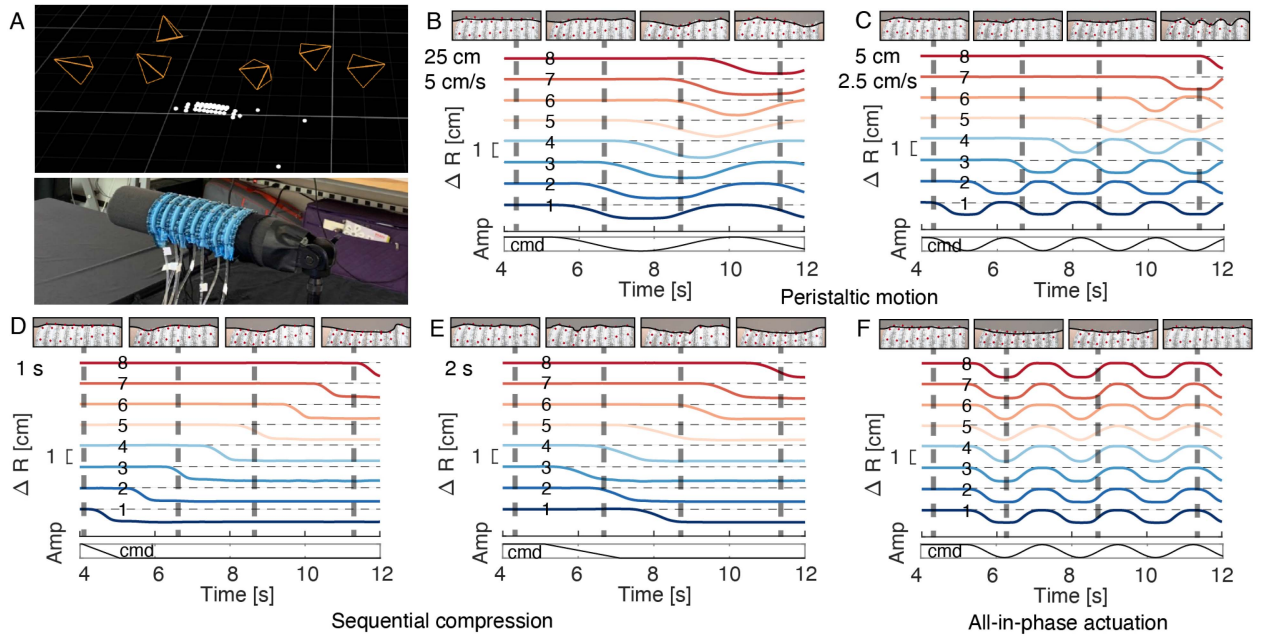

Fig. 6. To characterize the behavior of the peristaltic wearable robot, we wrapped it around a soft foam cylinder and applied dynamic peristaltic and non-peristaltic compression patterns (A). Motion capture results for various dynamic compression patterns with different wavelengths, wave speeds, and spatial patterns are shown, including peristaltic motions (B), (C), sequential compression with different compression durations and spatial patterns (pattern starts with actuator 1 in (D) and actuator 3 in (E)), and all-in-phase actuation (F). Annotations in the top left corner of each subfigure denote the wavelength λ and wave speed c of each peristaltic pattern, where frequency $f = \frac{c}{\lambda}$. The duration of the sequential compression patterns (1 s and 2 s respectively) are annotated in the top left for (D) and (E). Commanded amplitude inputs are shown below each pattern data plot and labeled as $'cmd'$.
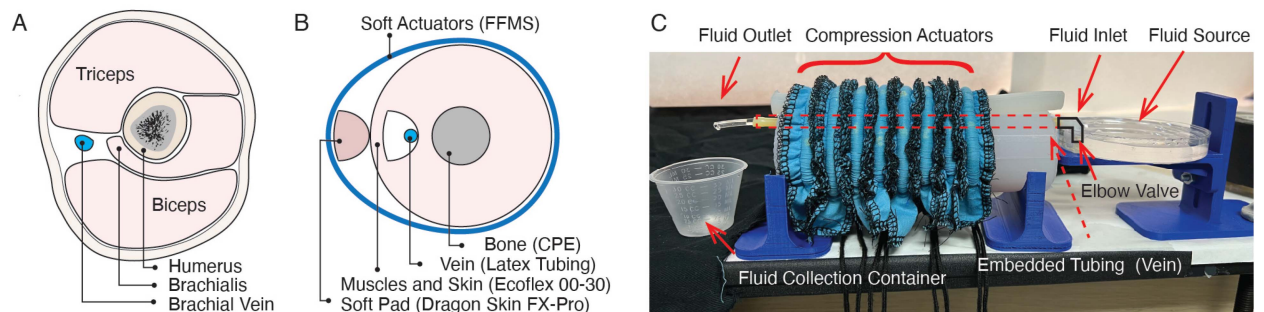

Fig. 7. The wearable robot is configured to promote hemodynamic circulation in a limb model via peristaltic transport. (A) A simplified illustration of the cross-section through the middle of the upper arm [33]. (B) The cross-section of the arm model used for the experiment. (C) Testing apparatus for the peristaltic transport.
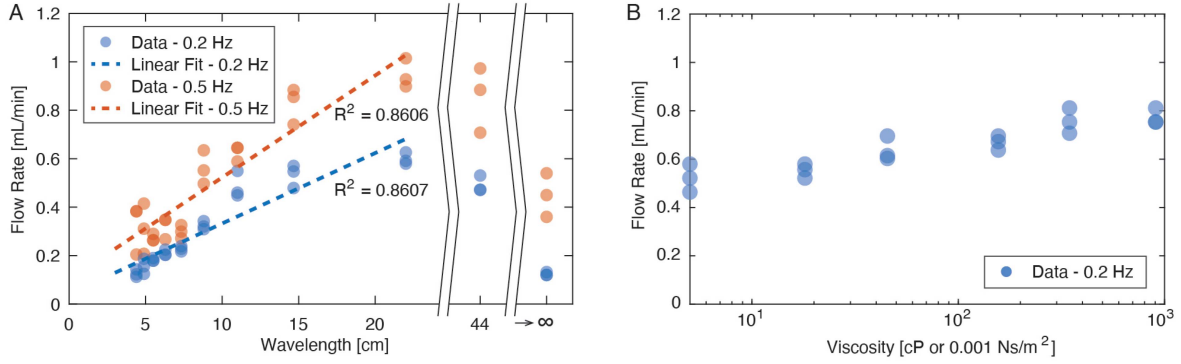
Fig. 8. (A) Experimental results of the flow rate showed a linear relationship with the wavelength, in agreement with the theoretical prediction (7). (B) Results showed that the viscosity had a weak effect on the flow rate, agreeing with the analytical predictions in [34], [35].

purely peristaltic, the time-averaged flow, $\bar{Q}$, in a tube depends on the average tube radius, a, the wave amplitude, b, and the wave speed, c, as follows:

$$\bar{Q} = \frac{\pi c b^2}{2} \frac{16a^2 - b^2}{2a^2 + 3b^2} \qquad (6)$$

When the frequency, f, of the peristaltic wave is constant, the time-averaged flow increases with wavelength, λ due to the increase in unoccluded volume:

$$\bar{Q} = \frac{\pi \lambda f b^2}{2} \frac{16a^2 - b^2}{2a^2 + 3b^2}, \quad \lambda = \frac{d}{ft} \qquad (7)$$

where d and t are the separation distance and the actuation time shift between adjacent actuators respectively. Frequencies of 0.2 Hz and 0.5 Hz were tested. Different peristaltic compression patterns were generated with onset delay time stepping between 0 ms (all-in-phase actuation) and 1125 ms (90° phase shift) by 125 ms (9° phase shift). Each wave pattern was repeated three times, and the fluid volume collected in the container was measured.

We found that the flow rate was higher for peristaltic motions than all-in-phase actuation when the wavelength was larger than about 5 cm. The time-averaged flow rate increased with the wavelength following a linear relationship (Fig. 8(a)), in agreement with theoretical predictions (7). The maximum flow rate was achieved when the wavelength was about 22 cm. When the wavelength further increased to 44 cm, the flow rate decreased. This may be due to the boundary conditions in the testing configuration, as the total length of actuation (about 9.2 cm) was much smaller than the wavelength of 44 cm. When the wavelength was very large, the wave pattern resembled all-in-phase actuation and the fluid reflux counteracting the peristaltic flow was large. This decrement for wavelengths above 22 cm was also presented when frequency increased to 0.5 Hz. The overall flow rate for 0.5 Hz was slightly larger than 0.2 Hz, in agreement with theoretical predictions (7).

The dynamic viscosity of glycerin at temperature 22 °C is about 1179 cP, which is much larger than the normal blood viscosity values (between 3.3 cP and 5.5 cP) [37]. Blood is also a non-Newtonian fluid whose viscosity changes depending on the hemodynamic conditions. Here, we evaluated the effect of fluid viscosity on induced flow rate. The viscosity of the transported fluid was varied by mixing glycerin with

TABLE II
THEORETICAL VISCOSITY AND REYNOLDS NUMBER OF GLYCERIN-WATER MIXTURES WITH DIFFERENT GLYCERIN CONCENTRATIONS IN MASS C_m

C_m	Density	Dynamic viscosity [cP]	Reynolds number
0.5	1.12	5.57	0.6427
0.7	1.17	20.88	0.1799
0.8	1.20	53.96	0.0714
0.9	1.23	193.24	0.0204
0.95	1.24	438.10	0.0091
1	1.26	1,178.64	0.0034

water at different weight percentages. The theoretical viscosity of the glycerin-water mixture was obtained using published results [36] (Table II).

Experimental results showed that viscosity had a weak effect on the flow rate (Fig. 8(b)). This finding is consistent with our theoretical predictions, which show that viscosity has little effect on flow rate when viscous forces are dominant (small Reynolds numbers) [34], [35]. We can expect that this system similarly enhances blood flow in a limb.

V. DISCUSSION AND FUTURE WORK

We present a compact peristaltic soft, wearable robot for robotic compression therapy. Although IPC devices have remained the main tool for automated compression therapy for decades, little device renovation has been done to improve the compactness, theoretical models, and spatiotemporal actuation due to limitations of pneumatic operation. We present a novel peristaltic wearable robot that employs a modular array of low profile hydraulic compression elements, whose widths are comparable to the human finger, and thus enable delivery of localized, dynamic compression. We also implement a modular hydraulic actuation system whose efficiency compares favorably to pneumatic devices. Each module is able to generate compression pressure up to 22 kPa and frequency up to 14 Hz, meeting requirements for compression therapy and therapeutic haptic massage [4], [12], [18]. Peristaltic compression patterns can be produced with programmable frequency, amplitude, phase delay, and duration. Thus, this system is capable of rendering a large range of spatial-temporal wave patterns. We further demonstrate the ability of this peristaltic, wearable system to promote peripheral circulation, and identify the optimum driving regime both theoretically and experimentally.

We empirically characterized the device's ability to drive fluid flow in a model limb via peristaltic transport, and provide a quantitative model with parameters governing the peristaltic pattern to the flow rate and fluid properties. These findings indicate that such systems may hold substantial promise for the treatment of lymphatic and blood circulation inefficiencies, which are associated with several health disorders. The model limb that was designed and fabricated for these experiments captures salient features of the circulatory system, but is in other respects quite different than a real arm. Although the systems we describe can readily be made portable (Fig. 3(f)), further miniaturization of the fluidic and electric source components could be achieved through a more specialized design focused on optimizing the motors, hydraulic reservoirs, batteries, and control electronics. Future translational research aimed at designing and evaluating the clinical efficacy of such a peristaltic robotic sleeve is warranted.

REFERENCES

[1] R. Duffield and J. Kalkhoven, "Effects of compression garments in strength, power and speed based exercise," in *Compression Garments in Sports: Athletic Performance and Recovery*. Berlin, Germany: Springer, 2016, pp. 63–78.

[2] H. Partsch, "Compression therapy: Clinical and experimental evidence," *Ann. Vasc. Dis.*, vol. 5, pp. 416–422, 2012.

[3] J. D. Crane et al., "Massage therapy attenuates inflammatory signaling after exercise-induced muscle damage," *Sci. Transl. Med.*, vol. 4, no. 119, 2012, Art. no. 119ra13.

[4] B. Partsch and H. Partsch, "Calf compression pressure required to achieve venous closure from supine to standing positions," *J. Vasc. Surg.*, vol. 42, no. 4, pp. 734–738, 2005.

[5] L. Roberts, "Effects of patterns of pressure application on resting electromyography during massage," *Int. J. Therapeutic Massage Bodywork*, vol. 4, no. 1, pp. 4–11, 2011.

[6] P. S. Moran, C. Teljeur, P. Harrington, and M. Ryan, "A systematic review of intermittent pneumatic compression for critical limb ischaemia," *Vasc. Med.*, vol. 20, no. 1, pp. 41–50, 2015.

[7] Y. M. Arabi et al., "Use of intermittent pneumatic compression and not graduated compression stockings is associated with lower incident VTE in critically ill patients: A multiple propensity scores adjusted analysis," *Chest*, vol. 144, no. 1, pp. 152–159, 2013.

[8] S. Kitayama et al., "Real-time direct evidence of the superficial lymphatic drainage effect of intermittent pneumatic compression treatment for lower limb lymphedema," *Lymphat. Res. Biol.*, vol. 15, no. 1, pp. 77–86, 2017.

[9] S. Zhao, R. Liu, C. Fei, and D. Guan, "Dynamic interface pressure monitoring system for the morphological pressure mapping of intermittent pneumatic compression therapy," *Sensors*, vol. 19, no. 13, 2019, Art. no. 2881.

[10] F. Manfredini et al., "Acute oxygenation changes on ischemic foot of a novel intermittent pneumatic compression device and of an existing sequential device in severe peripheral arterial disease," *BMC Cardiovasc. Disord.*, vol. 14, no. 1, pp. 1–10, 2014.

[11] G. W. John, A. J. Narracott, R. J. Morris, J. P. Woodcock, P. V. Lawford, and D. R. Hose, "Influence of intermittent compression cuff design on interface pressure and calf deformation: Experimental results," in *Proc. IEEE 29th Annu. Int. Conf. Eng. Med. Biol. Soc.*, 2007, pp. 2122–2125.

[12] C. J. Payne et al., "Force control of textile-based soft wearable robots for mechanotherapy," in *Proc. IEEE Int. Conf. Robot. Automat.*, 2018, pp. 5459–5465.

[13] W. L. Olszewski, P. Jain, G. Ambujam, M. Zaleska, M. Cakala, and T. Gradalski, "Tissue fluid pressure and flow during pneumatic compression in lymphedema of lower limbs," *Lymphat. Res. Biol.*, vol. 9, no. 2, pp. 77–83, 2011.

[14] A. J. COMEROTA, "Intermittent pneumatic compression for DVT prophylaxis," *Suppl. Endovascular Today*, vol. 10, pp. 3–5, 2011.

[15] T. A. Nakano and C. Zeinati, "Venous thromboembolism in pediatric vascular anomalies," *Front. Pediatrics*, vol. 5, 2017, Art. no. 158.

[16] A. McLeod, D. Brooks, J. Hale, W. Lindsay, R. Zuker, and H. THOMPSON, "A clinical report on the use of three external pneumatic compression devices in the management of lymphedema in a paediatric population," *Physiotherapy Canada*, vol. 43, no. 0003, pp. 00028–00032, 1991.

[17] M. Zhu, T. N. Do, E. Hawkes, and Y. Visell, "Fluidic fabric muscle sheets for wearable and soft robotics," *Soft Robot.*, vol. 7, pp. 179–197, 2020.

[18] K. Delis, Z. Azizi, R. Stevens, J. Wolfe, and A. Nicolaides, "Optimum intermittent pneumatic compression stimulus for lower-limb venous emptying," *Eur. J. Vasc. Endovascular Surg.*, vol. 19, no. 3, pp. 261–269, 2000.

[19] B. Wang et al., "Multiple blood flow surges during intermittent pneumatic compression: The origins and their implications," *J. Biomech.*, vol. 143, 2022, Art. no. 111264. [Online]. Available: https://www.sciencedirect.com/science/article/pii/S0021929022003050

[20] D. Guan, R. Liu, C. Fei, S. Zhao, and L. Jing, "Fluid–structure coupling model and experimental validation of interaction between pneumatic soft actuator and lower limb," *Soft Robot.*, vol. 7, no. 5, pp. 627–638, 2020.

[21] R. D. Sheldon, B. T. Roseguini, J. P. Thyfault, B. D. Crist, M. H. Laughlin, and S. C. Newcomer, "Acute impact of intermittent pneumatic leg compression frequency on limb hemodynamics, vascular function, and skeletal muscle gene expression in humans," *J. Appl. Physiol.*, vol. 112, no. 12, pp. 2099–2109, 2012.

[22] W. G. Paterson, "Esophageal peristalsis," in *GI Motility Online*, 2006. [Online]. Available: https://doi.org/10.1038/gimo13

[23] N. P. M. Kuijsters, W. G. Methorst, M. S. Q. Kortenhorst, C. Rabotti, M. Mischi, and B. C. Schoot, "Uterine peristalsis and fertility: Current knowledge and future perspectives: A review and meta-analysis," *Reprod. Biomed. Online*, vol. 35, no. 1, pp. 50–71, 2017.

[24] P. Edmond, J. A. Ross, and I. S. Kirkland, "Human ureteral peristalsis," *J. Urol.*, vol. 104, no. 5, pp. 670–674, 1970.

[25] J. Misra and S. Pandey, "Peristaltic transport of blood in small vessels: Study of a mathematical model," *Comput. Math. Appl.*, vol. 43, no. 8/9, pp. 1183–1193, 2002.

[26] M. Zhu et al., "PneuSleeve: In-fabric multimodal actuation and sensing in a soft, compact, and expressive haptic sleeve," in *Proc. CHI Conf. Hum. Factors Comput. Syst.*, 2020, pp. 1–12.

[27] M. Zhu, S. Biswas, S. I. Dinulescu, N. Kastor, E. W. Hawkes, and Y. Visell, "Soft, wearable robotics and haptics: Technologies, trends, and emerging applications," *Proc. IEEE*, vol. 110, no. 2, pp. 246–272, Feb. 2022.

[28] E. W. Hawkes, D. L. Christensen, and A. M. Okamura, "Design and implementation of a 300% strain soft artificial muscle," in *Proc. IEEE Int. Conf. Robot. Automat.*, 2016, pp. 4022–4029.

[29] P. T. Phan, M. T. Thai, T. T. Hoang, N. H. Lovell, and T. N. Do, "HFAM: Soft hydraulic filament artificial muscles for flexible robotic applications," *IEEE Access*, vol. 8, pp. 226637–226652, 2020.

[30] S. Kurumaya, H. Nabae, G. Endo, and K. Suzumori, "Active textile braided in three strands with thin McKibben muscle," *Soft Robot.*, vol. 6, no. 2, pp. 250–262, 2019.

[31] S. Kurumaya, H. Nabae, G. Endo, and K. Suzumori, "Design of thin McKibben muscle and multifilament structure," *Sensors Actuators A: Phys.*, vol. 261, pp. 66–74, 2017.

[32] R. L. Norton, *Design of Machinery: An Introduction to the Synthesis and Analysis of Mechanisms and Machines*, 3rd ed. New York, NY, USA: McGraw Hill, 2004, pp. 178–180.

[33] A. C. Eycleshymer and D. M. Schoemaker, *A Cross-Section Anatomy*. New York, NY, USA: D. Appleton, 1911.

[34] C. Barton and S. Raynor, "Peristaltic flow in tubes," *Bull. Math. Biophys.*, vol. 30, no. 4, pp. 663–680, 1968.

[35] M. Y. Jaffrin, "Inertia and streamline curvature effects on peristaltic pumping," *Int. J. Eng. Sci.*, vol. 11, no. 6, pp. 681–699, 1973.

[36] N.-S. Cheng, "Formula for the viscosity of a glycerol- water mixture," *Ind. Eng. Chem. Res.*, vol. 47, no. 9, pp. 3285–3288, 2008.

[37] E. Nader et al., "Blood rheology: Key parameters, impact on blood flow, role in sickle cell disease and effects of exercise," *Front. Physiol.*, vol. 10, 2019, Art. no. 1329.